HYDRODYNAMICS OF THRUST PRODUCTION IN A FISH-LIKE FLAPPING MEMBRANE

J.H.J. Buchholz* **J.M. Jiménez** **J.J. Allen**
A.J. Smits
Department of Mechanical and Aerospace Engineering, Princeton University
Princeton, NJ
∗buchholz@princeton.edu

DPIV and flow visualization were used to study thrust generation and the wake vortex structure for a flexible rectangular flapping membrane of aspect ratio 0.27. Two cables attached at the 1/4 chord point applied compressive forces and bending moments to the membrane which were coupled with hydrodynamic loads to approximate a traveling wave in the membrane. For Strouhal numbers (St) ranging from 0.38 to 2.58, a 2-P type structure was observed in the wake under both thrust- and drag-producing conditions. A simplified momentum analysis suggested a thrust coefficient increasing monotonically with Strouhal number and a transition from drag to thrust production at St approximately equal to 0.87. Kinematics of the vorticity are analyzed in streamwise planes in the near-wake and in spanwise planes on the body, and a three-dimensional model is proposed which connects vortex tubes identified in the different orientations.

1 Introduction

It has been speculated, (Gray, 1936), and recently established, (Anderson et al., 1998), that the efficiency of biologically inspired thrust production systems exceeds that of traditional quasi-steady motors. The performance of a variety of unsteady devices and analytical models to describe their behavior are presented in the reviews of Triantafyllou et al. (2000) and Wu (2001). The use of unsteady oscillating foils to produce thrust is by no means new. One of the earliest analyses of the thrust produced by an unsteady foil was performed by von Kármán and Burgess (1932). More recently Koochesfahani (1987) examined the flow structure produced by an oscillating airfoil in a low speed water channel over a range of reduced frequencies, f^*, where $f^* = fC/U$. Here C is the chord length of the airfoil, f is the frequency of oscillation and U is the freestream velocity. The principal results from this study were the identification of a change in the flow structure behind the foil, transitioning from a wake to jet as the flapping frequency f increased. A classic von Kármán street was seen when the foil acted as a drag producer and a reverse von Kármán street formed when thrust was being produced. Koochesfahani noted that the reduced frequency marking the transition between drag and thrust was affected by the amplitude of the oscillation. This suggests that the amplitude of flapping may be the more appropriate choice of length scale in a dimensionless parameter. Triantafyllou et al. (1993) defined a Strouhal number, St, using the excursion amplitude of the tail, A, such that $St = fA/U$. They were able to determine the Strouhal number where the maximum thrust coefficient and efficiency occurred. This was close to 0.3 and not critically dependent on the chord length. The physical basis for this result was explained in terms of convective and absolute instabilities. The thrust producing velocity profile is convectively unstable and hence when forcing is applied there is no competition with an absolutely unstable mode and the flow responds to the forcing frequency. Using typical thrust production velocity profiles they were able to compute the frequency that exhibited the most rapid rate of growth of the instabilities and found that it corresponded to a Strouhal number based on wake width (or maximum tail excursion) of $\simeq 0.3$. It should be noted that Liu and Kawachi (1999) reported a maximum efficiency at a Strouhal number of 0.72 for a tadpole swimming at a lower Reynolds number than in the work of Triantafyllou et al.

A similar methodology can be used to describe wake flows behind oscillating foils. In the literature related to vortex induced vibration the study of Williamson and Roshko (1988) noted a range of structural forms of the wake that were possible as a result of forcing a cylinder in cross flow. The effect of the forcing was a synchronization of the cylinder with the flow field and the formation of distinct wake patterns that were a function of the amplitude and frequency of forcing. These modes have been classified as 2-P and 2-S. Virtually identical 2-P and 2-S shedding modes have been seen behind oscillating airfoils in both thrust and drag production modes of Koochesfahani (1987).

In the case of a 2-P drag producing mode, Koochesfahani (1987) observed the vortex pairs inclined at an angle pointing upstream. When the Strouhal number was reduced by the increase of the free stream speed, for example, the jet was described as a 2-S mode and basically represents a reverse von Kármán street. In this mode, the formation of discrete vortex pairs was not observed.

In a seminal work on the swimming motion of slender fish, defined as a fish which makes small amplitude motions relative to the direction of locomotion, Lighthill (1960) was able to calculate expressions for the mean thrust produced by a fish as being equal to the difference between the work done by the fish and the kinetic energy that the fish imparts to the flow. The mean thrust was expressed as a function of the motion of the tail of the fish only. By careful consideration of the factors affecting his efficiency relationship Lighthill was able to deduce what characteristics the optimal swimming motions would most likely display; large amplitude oscillations at the tail only, a phase speed close to the free stream speed; and be comprised of at least one wavelength of reasonable amplitude. These conditions appear to be present in most live fish swimming examples.

Wu (1961) developed a linearized potential flow description of the flow field around a plate pinned at the leading edge executing a travelling wave motion. The full solution to the potential flow problem allowed Wu (1961) to calculate the unsteady thrust produced by the plate, the work done on the fluid by the flapping plate, and the efficiency. The principal results were a dependance of the swimming efficiency on the reduced frequency of the plate, defined as $k = \pi f C/U$. Wu (1961) also identified the reduced frequency at which the plate ceased to produce thrust and produced drag. Similar trends have been seen in Koochesfahani's experimental work, although the exact transition points have been found to be amplitude dependent. Since Wu (1961) proceeds on the assumption of infinitesimal amplitude this work is best used as a qualitative guide to the nature of the unsteady flow field.

Simplified models have been proposed suggesting that the 3-D wake structure produced by a swimming fish is a series of interconnecting vortex rings (Linden and Turner (2001)). Indeed recent experimental evidence for a vortex ring type structure forming downstream of a swimming mackerel was recently presented by Nauen and Lauder (2002). Perhaps the best current description of the 3D flow field comes from the panel method calculation of Zhu et al. (2002). This study focused on the complex interaction of the trailing vortices produced by the control fins of large fish with the large structures produced by the lunate tail. The resultant flow field somewhat resembles a series of interconnected vortex rings.

In the current experiment we aim to use a relatively simple actuation strategy to excite a membrane to oscillate in a travelling wave type motion. The aspect ratio of the membrane was of the order 0.3 and the aspect ratio based on tail excursion to span of membrane was of the order unity. The flow was therefore expected to be highly three dimensional. The membrane was excited by the application of a bending moment and compression force via a simple cabling system. The membrane was fixed at the leading edge and placed in a water channel. Experiments based on a slightly different actuation system were presented in Jiménez et al. (2003). Here, we present results over a much wider range of Strouhal numbers and describe the process of 3-D thrust production. Furthermore, the use of flexible thrusters that have the potential for energy storage and release has received little attention in the literature. The linearized potential flow calculations of Katz and Weihs (1978) showed the potential exists to improve unsteady thruster efficiency with the incorporation of an element of flexibility, and hence energy storage and release, to the foil. The current experiment offers a convenient mechanical set-up to investigate the effects of changing membrane stiffness.

2 Experiment

Experiments were conducted in a closed-loop water channel with test section dimensions of 0.46 m m wide by 0.33 m deep with a 3.5:1 contraction ratio and flow conditioning consisting of honeycomb and 6 screens. The membrane had a chord length C of 245 mm and a span S of 66 mm, giving an aspect ratio of 0.27. Its leading edge was fixed to the trailing edge of a symmetric fairing with 5 cm chord and 20% thickness. The method of attachment prevented displacement and rotation of the membrane

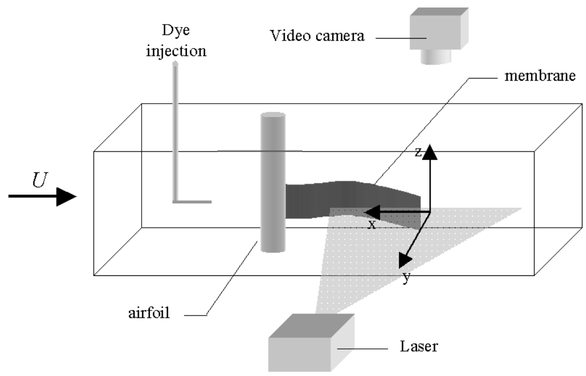

Figure 1: Experimental Setup.

at its leading edge. A stationary coordinate system is defined with the origin located at the mid-span and trailing edge of the undeformed membrane; see Figure 1.

A traveling wave with increasing downstream amplitude was approximated in the membrane by periodically actuating two cables which passed through the fairing and were attached to a pair of stepper-motor-driven cranks upstream and above the water channel. One cable was attached to each side of the membrane at $C/4$ in the streamwise direction and the mid-span as illustrated in Figure 2(a). The point of attachment was offset from the membrane surface by a distance of 5.6 mm. As a result, the cables produced moments and forces in the membrane as illustrated in Figure 2(b). Operation of the motors resulted in an approximately sinusoidal displacement of the cables in time. Hydrodynamic loading is essential in determining the membrane deformation; without it a very large-amplitude standing wave is produced when the membrane is actuated.

Data were acquired using Digital Particle Image Velocimetry (DPIV) and flow visualization. DPIV data in the x-y plane were used to assess the production of thrust or drag for the range of conditions studied, and to extract quantitative information about the wake structures. Flow visualization was used to obtain a more complete understanding of the vortex structure surrounding the membrane and in its wake.

DPIV experiments were conducted for Strouhal numbers (St) of 2.58, 1.88, 1.31, 0.87, 0.57, and 0.38. The Strouhal number was varied by varying the free stream velocity U and maintaining a constant forcing frequency of 0.9 Hz, resulting in Reynolds numbers based on membrane chord (Re_C) of 8×10^3, 1.2×10^4, 1.7×10^4, 2.7×10^4, 4.0×10^4, and 5.9×10^4. The flow was seeded with silver coated hollow spheres with mean particle diameter of 14 microns and true density of 1.7 g/cc. Images were acquired using a 120 mJ/pulse New Wave double-pulse Nd-YAG laser synchronized with a $2048\times2048\times12$-bit resolution pixel resolution Megaplus ES 4.0 CCD camera. A total of 38 images were captured at a rate of approximately 6 pairs per second for each of the 6 different Strouhal numbers studied. The flow was interrogated in a horizontal plane of dimensions $1.48C\times1.48C$ at the mid-span level ($z/C = 0$). The latter 20% of the membrane is visible in the images.

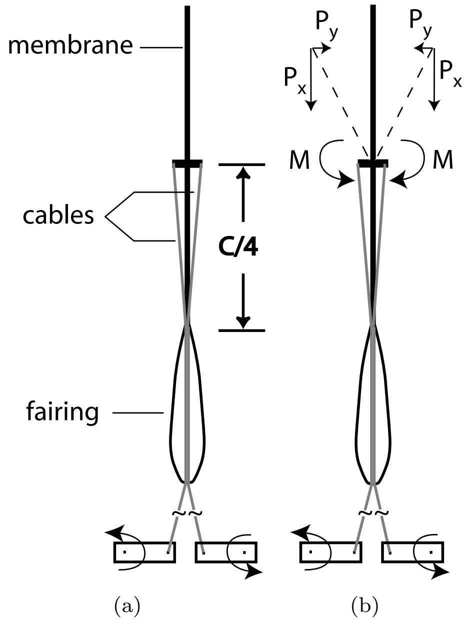

Figure 2: Attachment of actuating cables to the membrane (a), and the forces and moments applied by the cables (b).

Flow visualization was conducted with fluorescein and rhodamine B illuminated by an argon ion laser sheet. The two dyes were injected on opposite sides of the membrane to provide information about the origins of the material elements in the structures seen in the wake, and to aid in the connection of vortices seen in different image planes. Movies were obtained with a mini DV video camera, from which the images were extracted. The flow was investigated with the laser sheet aligned in positions parallel to the the x-y plane, the y-z plane, and also at a location rotated approximately 30 degrees from the x-z plane. These orientations, which are illustrated by hatched rectangles in Figure 3 will be referred to as *cross-stream*, *spanwise*, and *streamwise*, respectively.

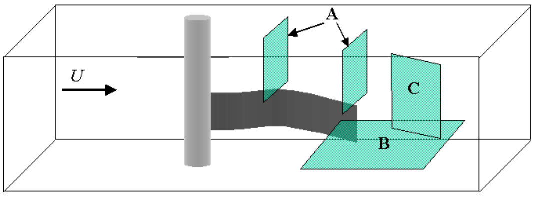

Figure 3: Flow visualization image planes. The cross-stream plane is the shaded rectangle(B). There are two spanwise planes (A); one at approximately $C/3$ and the other at the trailing edge. The streamwise plane (C) is oriented at approximately 30 degrees to the streamwise direction.

3 Results and Discussion

3.1 Membrane Kinematics

Figure 4 contains images of the membrane at five consecutive phases in the flapping cycle, separated by a time difference of $0.18T$, where $T = 1/f$. The black dots denote the crests and troughs in the membrane shape. A crest is defined as a local maximum (high point) and a trough is a local minimum (low point) in the shape of the membrane from the perspective of Figure 4. Figure 5 shows the locations of crests and troughs in the membrane's shape as functions of time over two flapping cycles. The major sources of error in these locations are glare and parallax in the images.

In each half-cycle, the membrane is deformed to produce a crest and a trough just upstream and downstream of the 1/4 chord point (Figure 4(c)). The upstream peak travels toward the fairing while the downstream peak rapidly accelerates toward the tail. The result of this acceleration can be visualized by noting the movement of the trough between Figures 4(c), 4(d) and in Figure 4(e) where it has propagated beyond the trailing edge. The amplitude A of the trailing edge at its mid-span was 100 mm ($0.4C$) $\pm 10\%$ throughout the range of conditions studied.

The membrane is responding to the combined loading of the applied moment and compressive force at the point and also the loading of the fluid. This means that a simplified model of the response of the membrane may be expressed using the Euler-Bernoulli beam equation with forcing:

$$\frac{\partial^2 y}{\partial t^2} - \kappa \frac{\partial^2 y}{\partial x^2} + \frac{EI}{m} \frac{\partial^4 y}{\partial x^4} = M(\frac{C}{4}) + f(x,t) \quad (1)$$

where $f(x)$ represents the fluid loading on the beam, E is Young's modulus, I the moment of inertia, m is the mass per unit length and $M(C/4)$ is the loading applied at the quarter chord point by the cables. Although the form of the loading is unknown and a complete solution for the shape of the membrane must come from coupling this equation to the equation for the fluid dynamics, see for example Fitt and Pope (2001), the Euler beam equation can be used to produce a set of modes that can be used to project onto the data set for an optimal description of the upstream/downstream travelling wave behavior of the beam. Such a technique was used by Allen and Smits (2001), and the use of Euler beam eigen functions to describe the stability of a coupled fluid structure interaction has its origins in the work of Paidoussis (1966), who considered the response of long flexible columns in axial flow.

3.2 Thrust Production

Instantaneous DPIV velocity and vorticity fields obtained in the near wake region of the flapping foil are shown in Figures 6 and 7 for $St = 1.88$ and 0.38, respectively. The spanwise vorticity ω_z has been nondimensionalized by the free-stream velocity and membrane chord length: $\omega_z^* = \omega_z C/U$. A convective velocity equal to the mean streamwise velocity has been subtracted from the instantaneous velocity vectors, making evident the presence of the shed vortices in each of these two figures. The areas of rotation visible in the transformed vector plots coincide with contours of high vorticity magnitude. A comparison of Figures 6 and 7 shows that the maximum wake vorticity magnitude for $St = 0.38$ is about one third of that for $St = 1.88$.

These velocity fields include the near wake region where the wake structure consists of shear layer vortices, which eventually coalesce to form a 2-P wake structure. The 2-P structure can be thought of as consisting of a series of vortex pairs, that create two unsteady jets, emanating from the tail of the flapping foil. In Figures 6 and 7 these multiple pair structures have been outlined with circles denoting the rotational orientation corresponding to each structure. They will be further discussed in the next section.

The DPIV data selected for display in Figures 6 and 7 correspond to conditions where maximum thrust and drag were generated respectively. Although the orientation of the vortices in the two figures appears to be similar, it is obvious that their non-dimensional strength is crucial in determining whether thrust or drag is generated.

In order to quantify the average thrust produced by the flapping membrane, the conservation of mo-

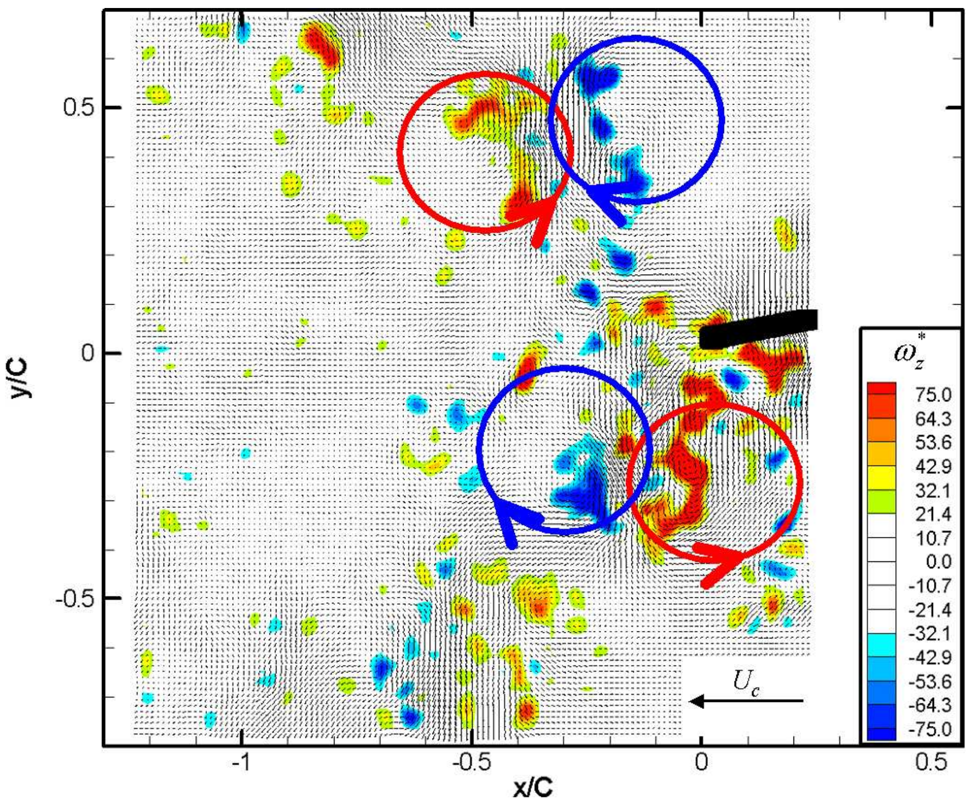

Figure 6: Instantaneous velocity field of near wake region of the flapping flexible membrane with nondimensional spanwise vorticity contour-plot background for aspect ratio $S/C = 0.27$, and $St = 1.88$. A constant velocity of $U_c = 1.46U$ is subtracted from the velocity in order to bring out the vortices more clearly.

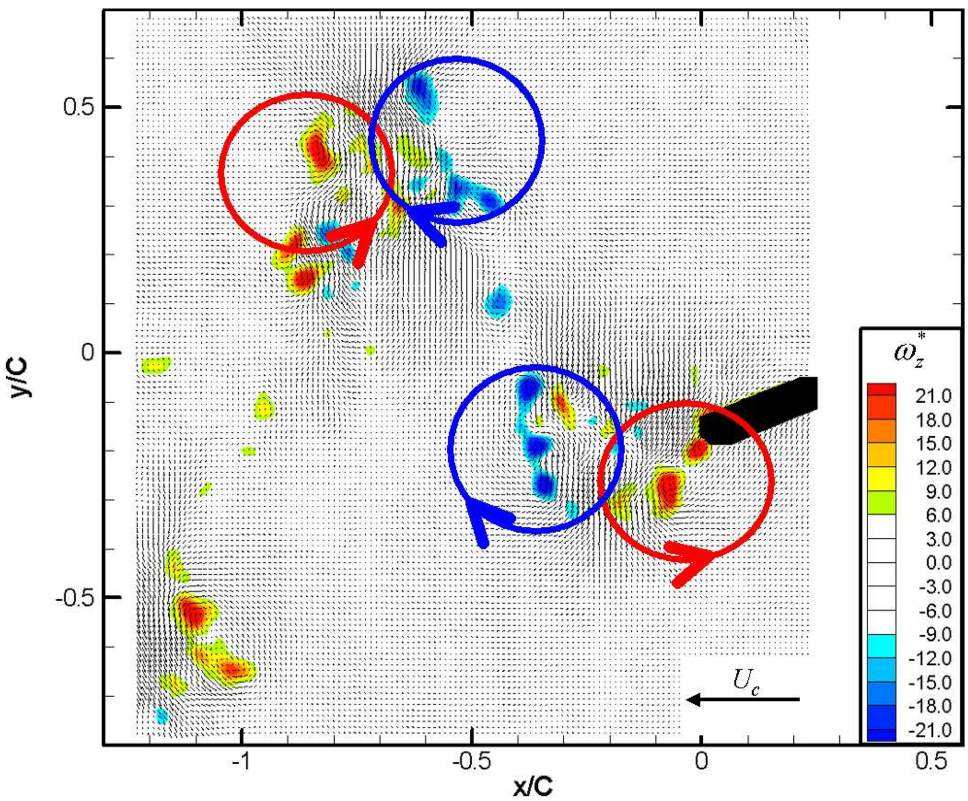

Figure 7: Instantaneous velocity field of near wake region of the flapping flexible membrane with nondimensional spanwise vorticity contour-plot background for aspect ratio $S/C = 0.27$, and $St = 0.38$. A constant velocity of $U_c = 0.93U$ is subtracted from the velocity in order to bring out the vortices more clearly.

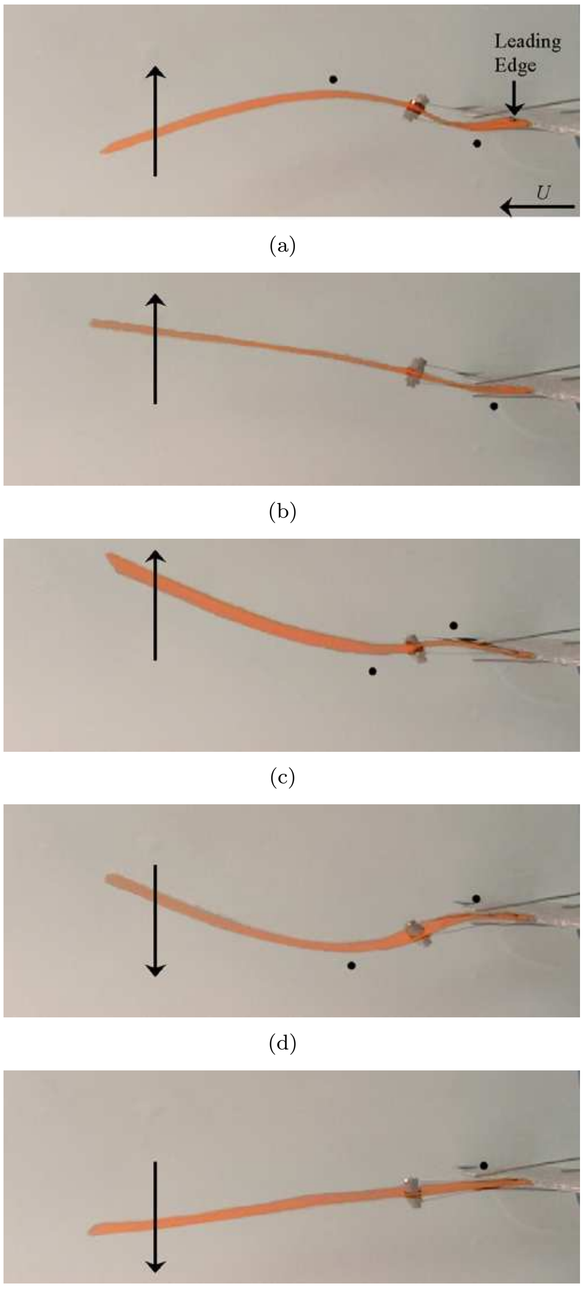

Figure 4: A cycle of membrane deformation. Images are separated in time by $0.18T$. Black dots denote the locations of crests and troughs. Flow is from right to left. Arrows denote direction of motion of the membrane.

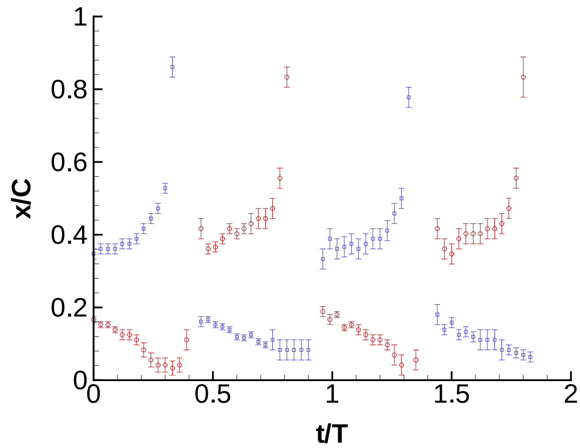

Figure 5: Locations of crests (○) and troughs (□) in membrane deformation as a function of time.

mentum for a fixed control volume was employed. The velocity distribution upstream of the fairing was assumed to be the uniform flow U, and downstream of the membrane wake is described as $u(y)$. The momentum balance of the steady (mean) flow over the flapping membrane is calculated under the assumptions that the pressures are equal on the upstream and downstream boundaries of the control volume, and that the flow is two-dimensional in the x-y plane. Applying mass conservation to the flux of momentum in the streamwise direction shows that the body exerts a force per unit depth on the fluid in the x direction with magnitude

$$T = \rho \int_{-\infty}^{\infty} u(y)(u(y) - U)\, dy, \qquad (2)$$

where ρ is the density of water and limits of integration in the cross-stream direction are $y = 0.7C$ and $-0.8C$. Note that the channel side walls are located at $y = \pm 0.94C$. The net flux of momentum per unit depth T is nondimensionalized by

$$q = \frac{1}{2}\rho U^2 A, \qquad (3)$$

giving a thrust coefficient C_T, where A is the peak to peak amplitude of the trailing edge of the membrane.

Mean velocity wake profiles for the six different Strouhal number cases studied were used to calculate nondimensional thrust profiles,

$$T^*(y) = \frac{\rho[u(y)(u(y) - U)]}{\frac{1}{2}\rho U^2 A}, \qquad (4)$$

across the streamwise plane normal to the z axis. The mean wake velocity profiles are constructed from temporal and spatial averages over 38 instantaneous velocity fields spanning over more than 7 flapping cycles.

Figure 8 shows the nondimensional thrust profiles $T^*(y)$ for the different Strouhal number cases studied for $-0.8 \leq y/C \leq 0.7$, and $z/C = 0$. A negative value of $T*$ indicates thrust and a positive value indicates drag. For the higher (thrust-producing) Strouhal numbers the $T^*(y)$ profile is characterized by two peaks approximately located at $y/C = \pm 0.35$. These two peaks correspond to jets produced by vortex pairs shed by the membrane, discussed above. As the Strouhal number decreases the magnitude of these peaks decreases resulting in a reduction of the momentum added by the jets.

Each profile is then integrated over y to give an indication of the magnitude of thrust T for the corresponding condition. The results of these integrations are presented in Figure 9(a). For $St = 2.58$, 1.88, 1.31, and 0.87, the mean thrust T shows a net addition of momentum (thrust generation), and $St = 0.57$ and 0.38, show a net momentum deficit. Figure 9(b) shows C_T as a function of Strouhal number. As the Strouhal number increases C_T increases. Figure 9(a) shows that the maximum amount of thrust is generated for the case when $St = 1.88$ but with a value of $C_T = 8.52$, which is about one-half that of $C_T = 17.06$ for $St = 2.58$.

These results should be regarded with some caution since we have investigated only a single plane in a complicated three-dimensional flow-field. However, because all data were obtained at a mid-span plane, it is expected that valid comparisons of thrust generation can be made between the different test conditions. Under this assumption, the greatest thrust is achieved for $St = 1.88$, and the greatest drag for $St = 0.38$. Past experiments at these relatively high Strouhal numbers, classified as "piston mode" have been cited as inefficient. Hence future experiments will focus on measurement of the energy imparted to the fluid by the membrane to determine if our 3-D thrust producer operates most efficiently in a regime that is significantly different to 2-D thrust producers.

Figures 10 and 11 show mean velocity vector fields for $St = 1.88$ and 0.38, respectively, with contours of the nondimensional mean streamwise velocity $\hat{u} = (u(y) - U)/U$ superimposed in the background. The free stream velocity has been subtracted from the mean streamwise velocity contours to emphasize the near wake flow characteristics of the flapping membrane. In Figure 10 two distinct jets are present from $-0.8 < x/C < 0$. Each jet is inclined at approximately 45° from the streamwise

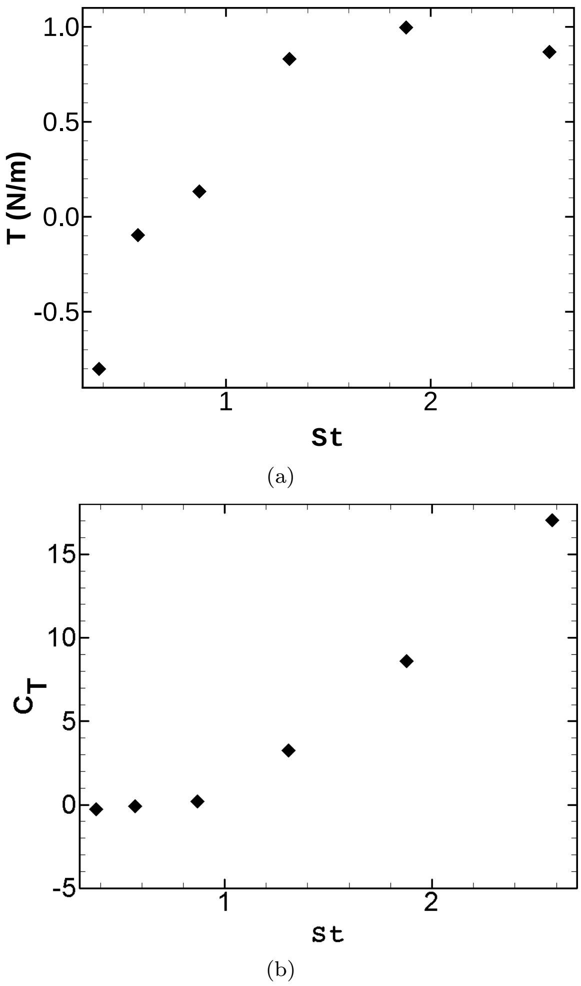

Figure 9: (a) Thrust per unit depth and (b) thrust coefficient as function of Strouhal number.

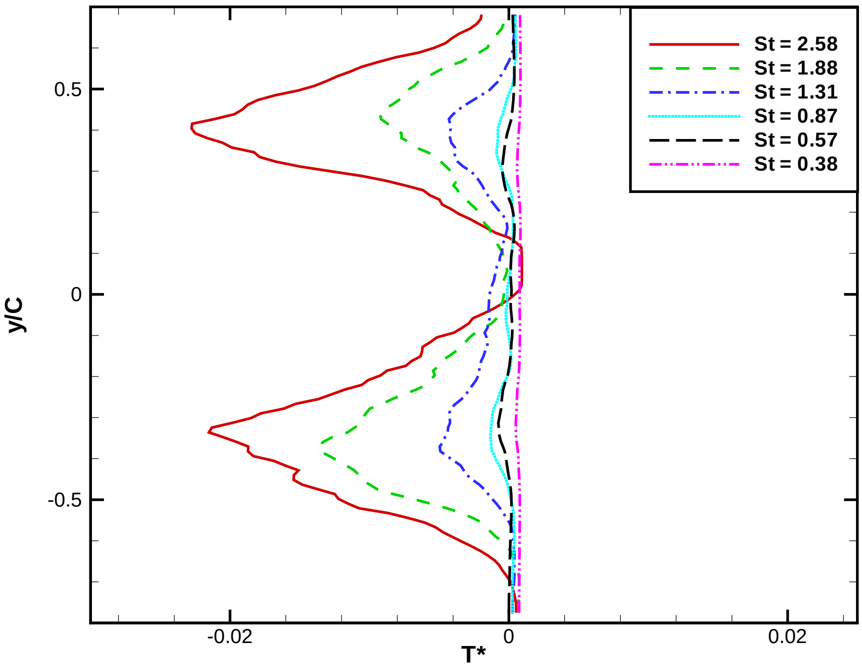

Figure 8: Nondimensional thrust profiles at $z/C = 0$ and $-0.8 \leq y/C \leq 0.7$ with aspect ratio $S/C = 0.27$, and $St = 2.58$, 1.88, 1.31, 0.87, 0.57, and 0.38. A negative value of T^* indicates thrust and a positive value indicates drag.

axis. For the thrust-producing cases, these jets also manifest themselves as peaks in the nondimensional thrust profiles of Figure 8. For $St = 0.38$ (Figure 11) the streamwise velocity contours reveal that the wake is dominated by drag. Two much weaker jets than those depicted in Figure 10 can be seen from $-1.2 < x/C < 0$, inclined at approximately 30° from the streamwise axis.

3.3 Wake Structure

The flow visualization images presented in this section were obtained at free stream velocities ranging from 0.08 to 0.1 m/s, corresponding to Reynolds numbers between 2.1×10^4 and 2.4×10^4 and Strouhal numbers between 1.08 and 0.92. These conditions have been chosen solely for the quality of the images obtained, and are within the thrust-producing range indicated by Figure 9. Fluorescein was injected at $y/C > 0$ and rhodamine B at $y/C < 0$. In additional flow visualization studies in which the free-stream velocity has been increased to produce Strouhal numbers below 0.3, we have not been able to infer any change in the basic topology of the wake structure.

In Figure 12, dye is injected at approximately the mid-chord and mid-span locations on either side of the membrane by means of 1.6 mm (outer diameter) stainless steel tubes. The tubes are positioned far enough away from the membrane to avoid collision with the flapping membrane. Although the dye is not, in general, injected directly into the boundary layer it is possible to make some observations about the origins of the wake vortices. The structures revealed by the DPIV data of Figures 6 and 7 can also be observed in the dye patterns of Figure 12. There is some mixing of colors in the wake vortices but in general, clockwise vortices are red and counterclockwise vortices are green.

As the trailing edge approaches the maximum deflection, vorticity is produced by the deceleration of the membrane, and vorticity of the same sign continues to be produced as the membrane subsequently begins to accelerate back toward its neutral position. In a complete cycle, this process produces the two upstream amalgamations of vorticity circled in Figures 6 and 7. One particular such stopping/starting event results in the creation of the green-dyed vortex of Figure 12(a). The green dye indicates that, although it persists in the wake at $y/C < 0$, its origin is the $y/C > 0$ side of the membrane, and its sense (counterclockwise) corresponds to the expected boundary layer vorticity on that surface.

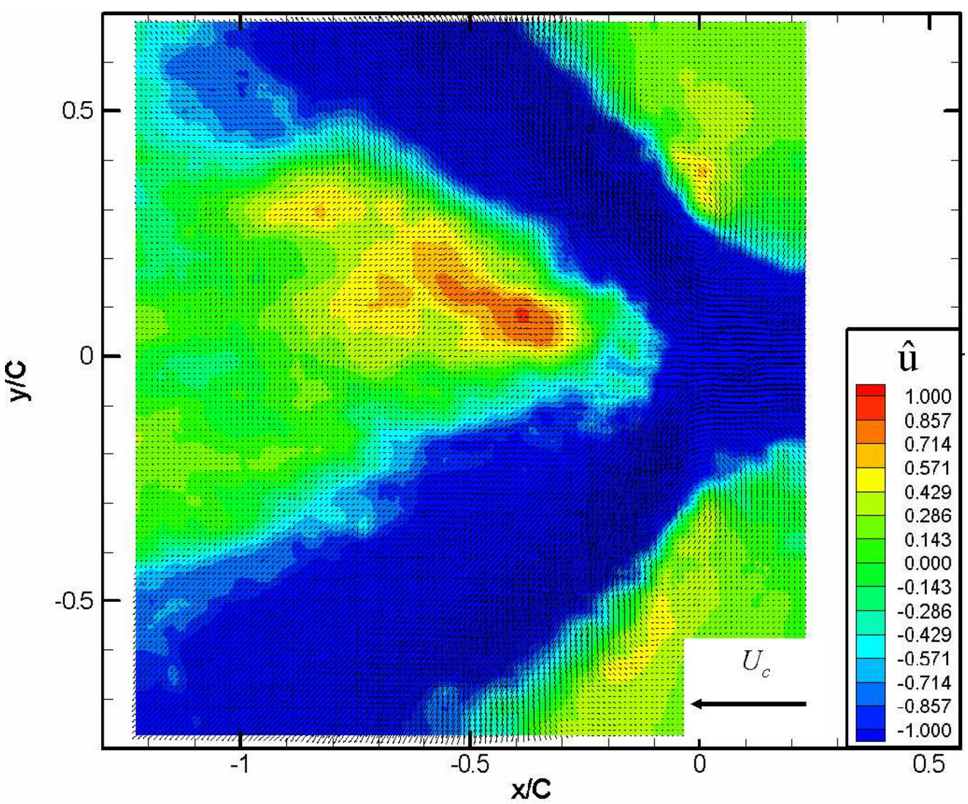

Figure 10: Mean Velocity field with nondimensional streamwise velocity global contour-plot as background for $-1.2 < x/C < 0.2$, $-0.8 < y/C < 0.7$ and $z/C = 0$, with aspect ratio $S/C = 0.27$, and $St = 1.88$. A constant velocity of $U_c = 1.0U$ is subtracted from the vector field.

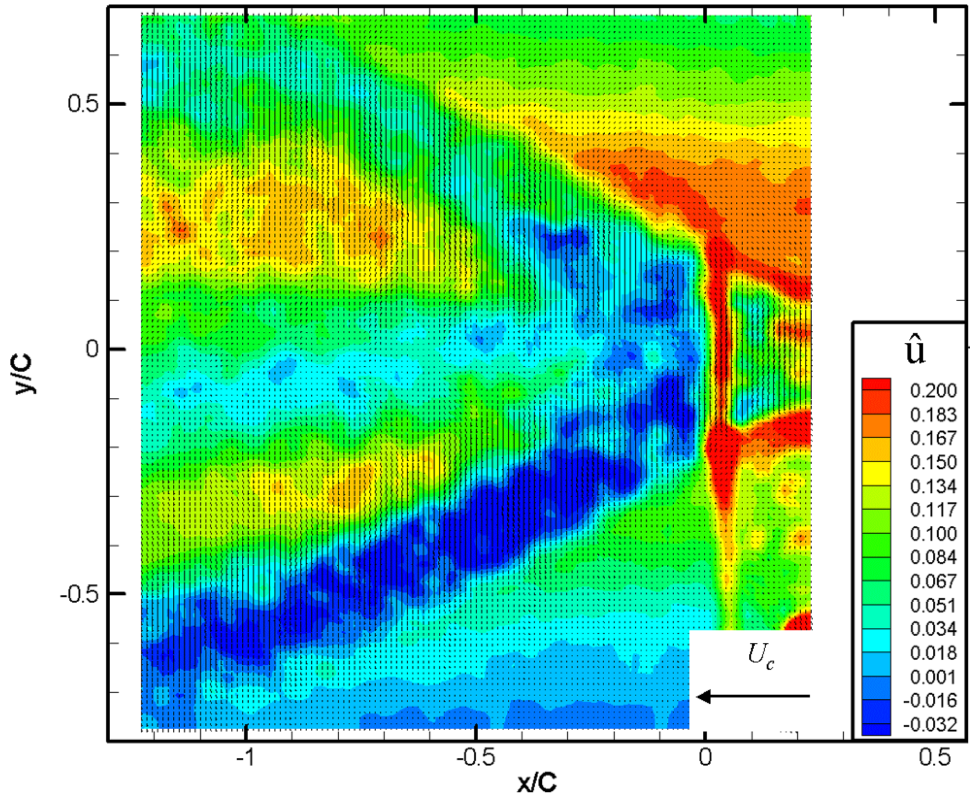

Figure 11: Mean Velocity field with nondimensional streamwise velocity global contour-plot as background for $-1.2 < x/C < 0.2$, $-0.8 < y/C < 0.7$ and $z/C = 0$, with aspect ratio $S/C = 0.27$, and $St = 0.38$. A constant velocity of $U_c = 1.0U$ is subtracted from the vector field.

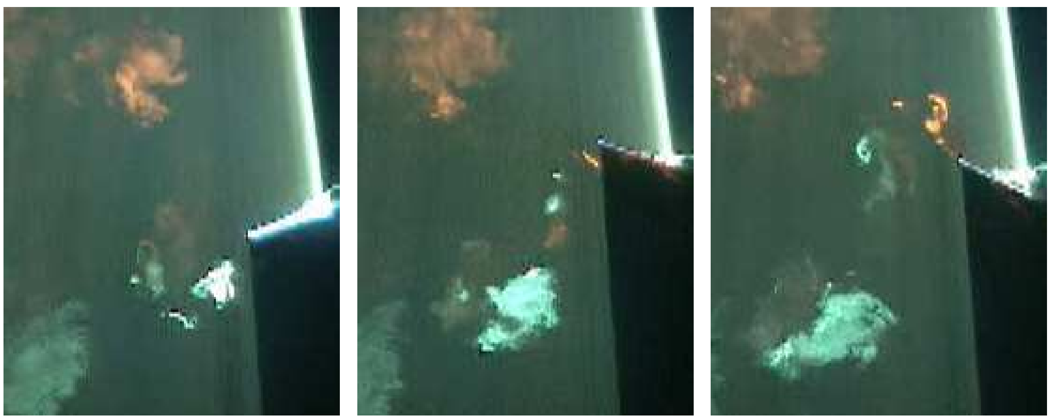

(a) Generation of stopping/starting vortex (green)

(b) Shedding shear layer

(c) Generation of stopping/starting vortex (red)

Figure 12: Generation of the 2-P structure in the cross-stream plane

As the trailing edge continues its sweep, vorticity of the same sign is shed in the form of a shear layer which does not appear initially to interact strongly with the stopping/starting vortex. This shear layer is evident in the concentrations of green dye which trace a line connecting the green stopping/starting vortex to the trailing edge of the membrane in Figure 12(b).

As the trailing edge approaches the opposite extreme, a stopping/starting vortex of the opposite sign is generated which forms a counter-rotating pair with the shear layer vorticity. This pair is shown in Figure 12(c) and is the basis for the 2-P wake structure presented in Figures 6 and 7.

Flow visualization in the spanwise plane reveals qualitatively the same evolution process in the streamwise vorticity along the chord of the membrane. Figure 13 shows a vortex pair formed in a spanwise plane located at approximately the 1/3 chord point with the membrane moving from left to right at the illuminated plane. In all of the spanwise visualizations, dye is injected on the surface of the fairing at $z/C = 0$. Figure 14 contains a sequence of spanwise images at the trailing edge, separated by intervals of 0.1 s ($0.09T$). In Figures 13 and 14 dye injection is moved upstream to the mid-chord of the fairing, and is at the level of the mid-span of the membrane. In this view, rhodamine B (red dye) is injected on the right of the membrane and fluorescein (green dye) is injected on the left. Figure 14(a) shows a second clockwise vortex (green), analogous to the shear layer vorticity in the cross-stream plane, formed as the trailing edge approaches the point of maximum excursion. This is followed by the generation of the stopping/starting vortex (red) in Figure 14(b) to form the vortex pair. The change in orientation of this pair is evident by comparing Figures 14(c) and 14(d), suggesting that the counterclockwise vortex (red) has greater circulation. Care needs to be taken when interpreting these images as the dominant component of flow velocity is normal to the page, hence the particles marked by the dye have typically acquired their angular momentum upstream of the field of view.

Visualization was also conducted in the streamwise plane with a vertical laser sheet rotated approximately 30° about a spanwise axis (This plane is labeled C in Figure 3). This orientation makes visible a cross section of the 2-P vortex pairs as they pass through the plane and helps to establish a link between the streamwise trailing vorticity and the 2-P structures seen in planform. Coherent structures resembling vortex rings can be seen traversing through the laser sheet. One of these structures is shown developing in Figure 15. The green dye (associated with the counterclockwise vortex in Figure 12) is diffuse compared to the bright red (clockwise) vortex core that has just been shed from the membrane. This is because the origin of the counterclockwise vortex is earlier in time. It would appear that the two structures , red and green, are connected across the top and bottom of the structures and this represents experimental evidence for the formation of vortex rings downstream of the trailing edge.

Figure 13: Streamwise vortex pair viewed in a spanwise plane at the 1/3 chord point

By comparing of the locations, colors, and senses of the dyed vortices in Figures 12 and 14, it appears that they are connected in the manner depicted in Figure 16. The suggested sequence of 3D vortex shedding and reconnection is sketched in Figure 16. The first image shows a 3D representation of the shedding of a counter clockwise vortex, including the streamwise filaments that connect the main core to the flapping plate. The 2D view one would expect to see from above is sketched to the right. The second figure shows the formation of the stopping (clockwise) vortex at the end of the downstroke. By a relatively simple technique of requiring that all vortex filaments have their origin at the membrane surface it can be see that this process should produce a complex interaction of opposite signed vorticity above and below the flapping membrane. The third image in the sequence shows the continual generation of clockwise vorticity while the stopping vortex and downstroke vortex convect downstream with weakening of the opposite signed streamwise vorticity due to their close proximity. The fourth image shows the merging and reorientation of the

(a) Roll-up of (green) shear-layer vorticity (c.f. Figure 12(b).

(b) Generation of (red) stopping/starting vortex (c.f. Figure 12(c)).

(c) Continued generation of stopping/starting vortex.

(d) Rotation of pair.

Figure 14: Generation of the 2-P structure in the spanwise plane. The laser sheet is located at the trailing edge of the membrane. Images are separated by a delay of 0.1s ($0.09T$).

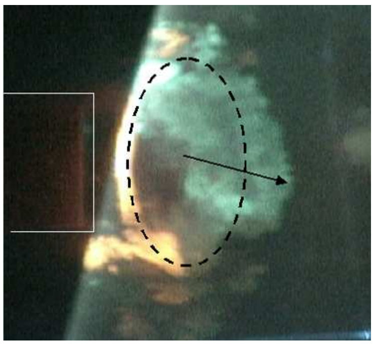

(a)

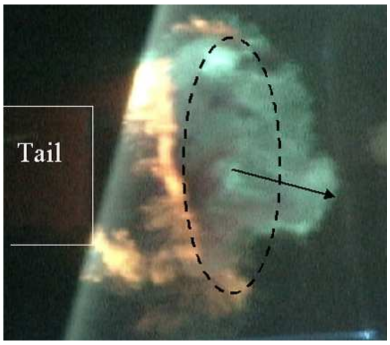

(b)

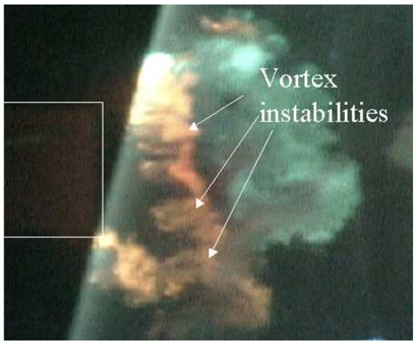

(c)

Figure 15: Wake structures viewed in a vertical plane oriented approximately 30° from the streamwise direction. The upstream edge of the light sheet is approximately 5 cm closer than the centerline of the membrane. The flow is from left to right. The sequence shows the formation of a vortex ring and the development of instabilities on the ring

streamwise vortices in a pinching-off process and results in the formation of a ring-like structure. The sketches in the right hand column shows how the 2P structure correlates with the ring formation process.

Furthermore, observation of digital video sequences shows a complex distribution of vorticity normal to the plane of observation within the fluorescein. Vortex filaments on the main vortex cores are highlighted in Figure 15(c). This appears to be the formation of a short wave vortex instability that eventually leads to breakdown of the primary structures. The calculations of Kransy (1987), examining the stability characteristics of a trailing vortex sheet from a delta wing show similar structures to those highlighted in Figure 15(c).

In the present case, a full description of this model for the vortex skeleton will require further characterization of the membrane motion, and more accurate information linking photographs to the phase of the membrane cycle. It should be noted that as the free-stream velocity was increased well into the drag-producing range of Figure 9, visualization in the cross-stream plane (at $z/C = 0$) was consistent with the structure shown in Figure 16. That is, the signs of the vortices did not reverse as would be expected for the generation of drag. Clearly, the wake is highly-three-dimensional, and more experiments and momentum analyses must be conducted to produce a consistent model relating wake structure and thrust production and efficiency.

4 Conclusions

The simple momentum analysis conducted in this study suggests the production of thrust for $0.87 \leq St \leq 2.58$, and drag for $0.38 \leq St \leq 0.57$. This differs substantially from the results of Triantafyllou et al. (1993). In the present experiment, the momentum analysis indicates a net drag force at the Strouhal number where they obtained optimal thrust. In the entire range of Strouhal numbers studied, flow visualization indicates the presence of a 2-P wake structure which is connected to an analogous structure visualized along the body in a spanwise plane and results in what appears to be a vortex ring type structure downstream of the flapping foil. For Strouhal numbers ranging between 0.3 and 2.58, no transition to a 2-S structure was observed, as in the experiments of Koochesfahani (1987).

5 Acknowledgements

This work was supported by the Office of Naval Research. The authors thank Mr. S. Santiago for his assistance in the construction of the experimental apparatus.

References

J.J. Allen and A.J. Smits. Energy harvesting eels. *J. Fluid. Struct.*, 15:629–640, 2001.

J.M. Anderson, K. Streitlien, D.S. Barrett, and M.S. Triantafyllou. Oscillating foil of high propulsive efficiency. *J. Fluid Mech.*, 360:41–72, 1998.

A.D. Fitt and M.P. Pope. The unsteady motion of two-dimensional flags with bending stiffness. *J. Engrg. Math.*, pages 227–248, 2001.

J. Gray. The propulsive powers of the dolphin. *J. Exp. Biol.*, 13:192–199, 1936.

J.M. Jiménez, J.H.J Buchholz, A.E. Staples, J.J. Allen, , and A.J. Smits. Flapping membranes for thrust production. In *Integrated Modeling of Fully Coupled Fluid-Structure Interactions Using Analysis, Computations, and Experiments*, 2003.

J. Katz and D. Weihs. Hydrodynamic propulsion by large amplitude oscillation of an airfoil with chordwise flexibility. *J. Fluid Mech.*, 88:485–497, 1978.

M.M. Koochesfahani. Vortical patterns in the wake of an oscillating airfoil. In *AIAA paper 87-0111*, 1987.

R. Kransy. Computation of vortex sheet roll-up in the treffetz plane. *J. Fluid Mech.*, 184:123–156, 1987.

M.J. Lighthill. Note on the swimming of a slender fish. *J. Fluid Mech.*, 9(2):305–317, 1960.

P.F. Linden and J.S. Turner. The formation of optimal vortex rings, and the efficiency of propulsion devices. *J. Fluid Mech.*, 427:61–72, 2001.

H. Liu and K. Kawachi. Vortical patterns in the wake of an oscillating airfoil. *J. Comput. Phys.*, 155:223–247, 1999.

J.C. Nauen and G.V. Lauder. Hydrodynamics of caudal fin locomotion by chub mackerel. *J. Exp. Biol.*, 205:1709–1724, 2002.

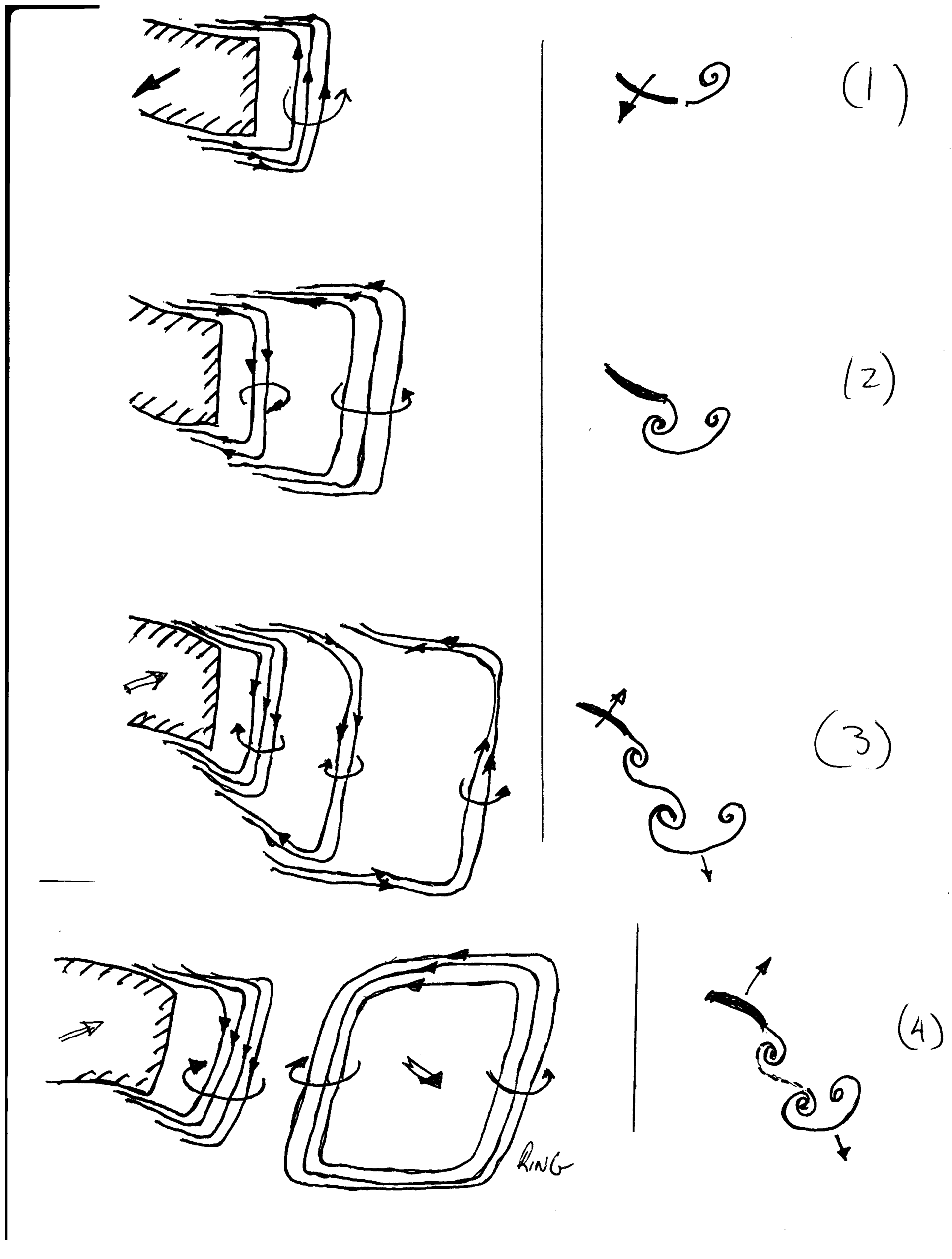

Figure 16: Schematic of the formation of vortex rings via a combination of the 2-P structure and trailing vortices

M. Paidoussis. Dynamics of flexible slender cylinders in axial flow. part 1. theory. *J. Fluid Mech.*, 26:717–736, 1966.

G.S. Triantafyllou, M.S. Triantafyllou, and M.A. Grosenbaugh. Optimal thrust development in oscillating foils with application to fish propulsion. *J. Fluid. Struct.*, 7:205–24, 1993.

M.S. Triantafyllou, G.S. Triantafyllou, and D.K.P. Yue. Hydrodynamics of fishlike swimming. *Annu. Rev. Fluid Mech.*, 32:33–53, 2000.

T. von Kármán and J.M. Burgess. *General aerodynamic theory: perfect fluids. In Aerodynamic Theory, Vol. II (ed. W. F. Durand)*. Springer Verlag, Leipzip, 1932.

C.H.K. Williamson and A. Roshko. Vortex formation in the wake of an oscillating cylinder. *J. FLuid. Struct.*, 2:355–381, 1988.

T.Y. Wu. Swimming of a waving plate. *J. Fluid Mech.*, 10(3):321–344, 1961.

T.Y. Wu. On theoretical modeling of aquatic and aerial animal locomotion. *Adv. in Appl. Mech.*, 38:291–353, 2001.

Q. Zhu, M.J. Wolfgang, D.K.P. Yue, and M.S. Triantafyllou. Three-dimensional flow structures and vorticity control in fish-like swimming. *J. Fluid Mech.*, 468:1–28, 2002.